Effect of Silicon on CGHAZ Toughness and Microstructure of Microalloyed Steels

R. TAILLARD, P. VERRIER, T. MAURICKX, and J. FOCT

The aim of this article is to present the beneficial effect of a reduction of silicon content on coarse-grained heat-affected zone (CGHAZ) toughness. This study was achieved with experimental and industrial E355 structural steels. These 0.09 wt pct C steels were Ti-microalloyed with silicon contents ranging from 0.05 to 0.5 wt pct. First, we demonstrate that the CGHAZ toughness is predominantly affected by the volume fraction of retained austenite (γr). Second, we show that the existence of retained austenite pertains only to its carbon enrichment. This enrichment is promoted essentially by an increase of the silicon level due to the retarding action of silicon on the formation of carbides in ferrite as well as in austenite. In the same way, the increase of silicon content slows down the decomposition of retained austenite into pearlite. The reduction of the silicon content of the steel greatly increases the ductility of the CGHAZ through the decrease of the volume fraction of retained austenite.

I. INTRODUCTION

THE increasingly severe environment of offshore petroleum sites has spurred metallurgists to improve structural steels. In order to be used, the steels must satisfy stringent requirements for the base metal and, particularly, in the weldments. Cold cracking and low toughness levels are two major problems induced by welding operations.[1,2] These two phenomena may occur in the coarse-grained heat-affected zone (CGHAZ) following short or long cooling times, respectively. At intermediate cooling times, *i.e.*, intermediate welding energy and/or plate thickness,[1] welding may be conducted safely. The extension of this safe welding domain governs the development of new steels.

During welding, structural changes and phase transformations occur in the heat-affected zone (HAZ), which determine its mechanical properties[1,2] and, more particularly, the loss of toughness in the CGHAZ formed at the highest welding energies. Figure 1 illustrates the parameters that affect the CGHAZ toughness. This synoptical diagram can be divided in three main parts. The connection (I) is well defined by means of Rosenthal equations established in 1946.[3] The study of the relationship (III) shows that among the parameters likely to act on the CGHAZ toughness, retained austenite (γr) exerts a predominant and harmful effect.[4,5,6] However, the retained austenite is at least partially transformed into martensite during testing. The mechanical destabilization of retained austenite depends on its carbon content, on its morphology, and on the test temperature.[6,7] This martensite-austenite constituent (MAC) gives rise to concentration and triaxiality of stresses at the interface in the ferritic matrix. This stress-raising effect leads to the brittle fracture by cleavage of the matrix of ferrite.[6,7,8]

The aim of the present study was to investigate the relationship between chemical composition and microstructure (II) and, especially, the effect of silicon on the CGHAZ microstructure and toughness of microalloyed steels. Finally, we propose a steel composition that exhibits very high toughness at low temperatures.

II. MATERIALS AND EXPERIMENTAL PROCEDURE

A. *Base Metal*

Steels A through D were laboratory castings, while alloy E was industrially manufactured. The 12-mm-thick plates of steels A through D, on the one hand, and the 50-mm-thick plate of steel E, on the other hand, were obtained by distinct controlled rolling and accelerated cooling processes. Alloys A through D were produced as a 60-kg heat that was cast in four ingots. The silicon content of each ingot was then adjusted by pure silicon additions to the compositions shown in Table I. According to this manufacturing process, the chemical compositions of these only Ti-microalloyed materials differ essentially by their silicon content over the 0.050 wt pct to 0.500 wt pct range. The silicon content of alloy E was chosen according to the results obtained with steels A through D. In addition, the balance between the concentrations of Ti and N in steel E was selected so as to maximize the heterogeneous nucleation of acicular ferrite on intragranular TiN precipitates.[9,10] Moreover, the levels of phosphorus and sulfur were rather low, amounting respectively to maxima of 80 ppm and 28 ppm for steel E. The mechanical behavior was generally investigated using subsurface specimens manufactured in the long transverse direction of the plates. Table II gives the mechanical properties of the base materials. Considering the low thicknesses of the plates, the mechanical properties of each steel result primarily from the changes of chemical composition and, for alloy E,

R. TAILLARD and J. FOCT, Professors, are with the Physical Metallurgy Laboratory, U.R.A. C.N.R.S. No. 234, University of Lille, 59655 Villeneuve d'Ascq, France. P. VERRIER and T. MAURICKX, formerly Graduate Students, Physical Metallurgy Laboratory, University of Lille, are Research Engineers, Centre de Recherches et de Développement Métallurgiques, Sollac, 59381 Dunkerque, France.

Manuscript submitted October 25, 1993.

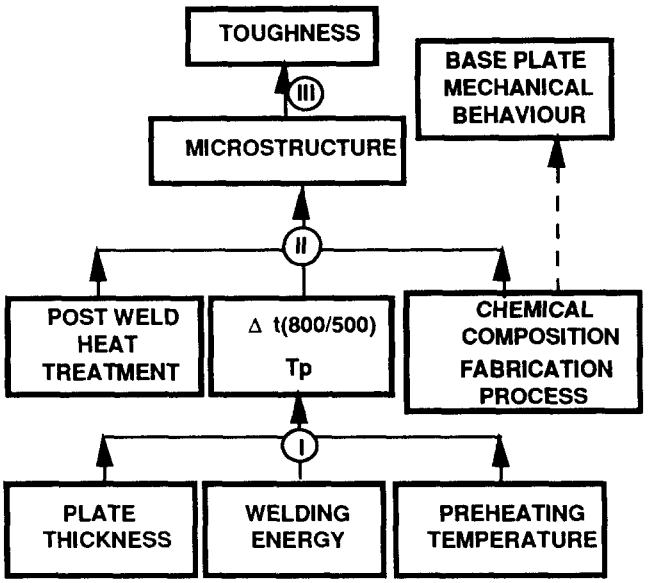

Fig. 1—HAZ toughness parameters.

Table I. Chemical Composition (Weight Percent) of the Materials

Steel	C	Mn	Ni	Ti	N	Si
A	0.075	1.55	0.45	0.010		0.050
B	to	to	to	to		0.104
C	0.090	1.60	0.50	0.015	0.002	0.245
D						0.500
E	0.090	1.50	0.47	0.012	0.003	0.095

thermomechanical processing. In particular, it is important to note that for steels A through D, which were processed in a similar manner, a linear increase of approximately 30 and 45 MPa in proof and tensile strength are observed for an increase in Si concentration from 0.05 to 0.5 wt pct.

B. *Simulations Conditions*

The steels were studied after thermal cycles that simulate the CGHAZ thermal history. The samples were resistance-heated using a Gleeble 1500 thermomechanical simulator. The thermal cycles, defined in Table III and shown in Figure 2, were computed from the three dimensional heat-flow equations of Hannerz.[11] These cycles are defined by a peak temperature (T_p) and by a cooling time (Δt) between 1073 K (800 °C) and 773 K (500 °C). The peak temperature depends both on the distance from the fusion line and on heat input. The 1623 K (1350 °C) T_p value is typical of the CGHAZ. This peak temperature was reached with a 400 K/s heating rate. In the present work, the cooling time (Δt) increases only with welding energy. The width of the simulated HAZ was close to 5 mm.

C. *Mechanical Testing*

Mechanical properties were characterized by Vickers hardness (H_V) measurements and Charpy V impact notch (CVN) testing. The Charpy V specimens were of standard dimensions. Their notch was cut perpendicularly to the plate surface and located abreast of the soldering of the thermocouple of control, *i.e.*, in the middle of the simulated CGHAZ.

Table II. Mechanical Behavior of Base Alloys

Steel	YS* (MPa)	TS* (MPa)	e_f^*	Kv (−80 °C)* (J)
A	405	500	36	345
B	406	490	35	340
C	415	515	34	335
D	435	540	33	320
E	360	470	34	170

*YS = 0.2 pct proof stress, TS = tensile strength, and e_f = tensile elongation at fracture (pct). This value is measured by using standard tensile specimens, whose original gage length L_0 and original cross-sectional area S_0 obey the relationship: $L_0 = 5.65 \cdot (S_0)^{1/2}$, Kv · (−80 °C) = Charpy impact energy at −80 °C.

Table III. Weld Thermal Simulation Programs

Welding Energy (kJ/mm)	Preheating or Interpass Temperature (°C)	Δt (s)	T_p (°C)
0.7	—	4	
1.25	—	12	
2.5	—	40	1350
5.0	100	120	

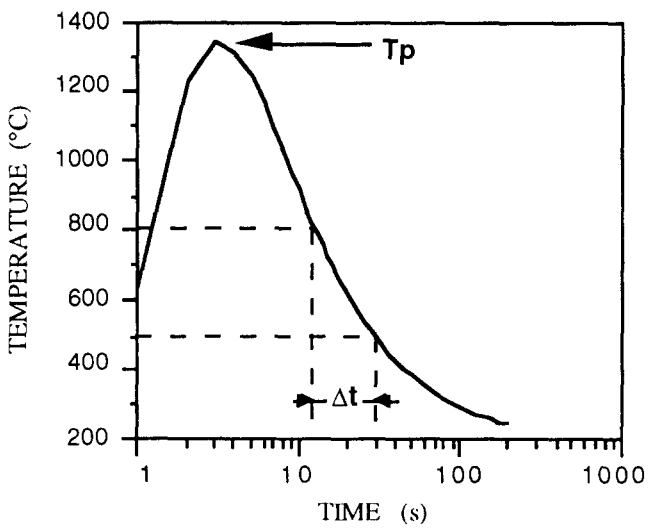

Fig. 2—Shape of the thermal cycles used to simulate the CGHAZ thermal histories.

D. *Microstructural Investigation*

Microstructural analyses were carried out by X-ray diffractometry, Mössbauer spectrometry (MS), light microscopy, scanning electron microscopy (SEM) and thin foil transmission electron microscopy (TEM). The percentages of the various constituents are accurate to

±5 pct. They were determined by planimetry on light micrographs. The differentiation of the phases was based on their salient microstructural features, *i.e.*, the existence of parallel laths separated by an interlath phase in lath upper bainite, which differ from both the disorientated packets of laths in martensite, the more equiaxed grains in acicular ferrite, and the γ grain boundary localization of proeutectoid ferrite. The Mössbauer spectra were obtained at room temperature in transmission and constant accelerated mode using a cobalt 57 source and 30-μm-thick specimens with a 10^{-4} m^2 area. The velocity origin corresponds to the average of the speeds of the Fe_α peaks. The method of spectra analysis has already been published.[12] The investigations by transmission electron microscopy were made using a JEOL* 200 CX equipped with energy-dispersive spectrometry (EDX). The TEM specimens were mechanically polished to a thickness of 70 μm and then thinned in an automatic jet-polishing apparatus operating at 13 °C and at a current density of 4.10^{-5} A/m^2. The electrolyte was composed in volume of 95 pct glacial acetic acid plus 5 pct perchloric acid.

*JEOL is a trademark of the Japan Electron Optics, Ltd, Tokyo, Japan.

III. RESULTS

This section deals with the mechanical behavior and microstructure of the simulated CGHAZ of the laboratory alloys A through D. As suggested by Figure 1, microstructural investigation is necessary to explain the influence of welding energy and silicon content upon the mechanical properties.

A. *Mechanical Behavior*

Figure 3 displays the continual and marked softening of the CGHAZ with increasing heat input. Moreover, at any cooling rate (heat input), the hardness of the CGHAZ generally increases with increasing silicon content.

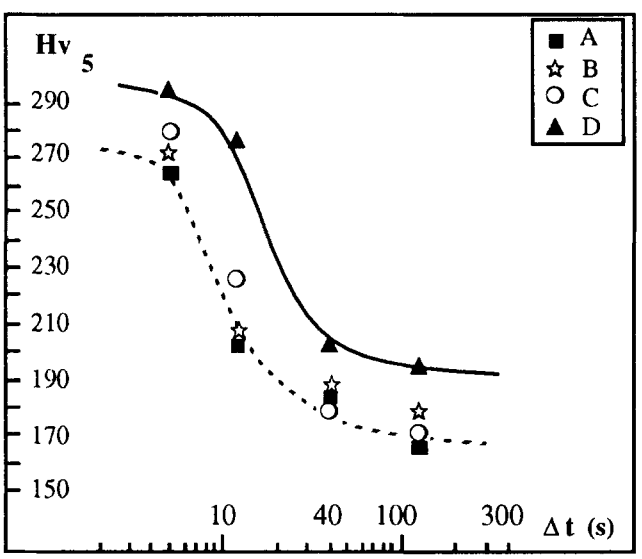

Fig. 3—Relationship between cooling time and hardness of the CGHAZ.

Furthermore, the ductile-brittle transition temperatures reported in Figure 4 indicate improvement in CGHAZ toughness with the reduction of the silicon content and with increasing welding energy. This unusual effect of welding energy on toughness is more evident the lower the silicon addition. The Charpy V transition temperatures are at most equal to −50 °C or −25 °C for a fracture energy of 28 or 100 J, respectively.

B. *Metallography*

It is relevant to note that the microstructures of the alloys are significantly modified by an increase in Δt. This feature is illustrated by Figure 5 for the case of steel B and quantified in Table IV by the fraction of each microstructural constituent in each heat-affected zone. The microstructure exhibits the conventional evolution of the E 355 grade of microalloyed steels[2,4,5,13,14] and varies from a mixture of martensite (M) and lath upper bainite (LUB) for the highest cooling rate (Δt = 4 s) to a duplex structure comprised of allotriomorphic proeutectoid ferrite (PF) and acicular ferrite (AF) for the lowest cooling rate (Δt = 120 s). As illustrated by the transmission electron micrographs in Figure 6(b) and described by the authors,[9] acicular ferrite is a medium-quenched structure composed of heavily dislocated and equiaxed grains characterized by a length-to-width ratio lower than 4. Moreover, Table IV indicates a small increase of the steels' hardenability with their silicon content. Furthermore, it should be noticed that these phase transformations occur without a change in prior austenite grain size (d_γ). Regardless of the steel chemical composition and the welding energy, the average value of d_γ remains constant and close to 75 μm. This constancy of d_γ results from the microaddition of titanium.

At low welding energies ($\Delta t \leq 12$ s), optical microscopy and SEM display the presence of elongated particles in the boundaries of lath upper bainite (Figures 5(a) and 6(a)). Alternatively, at higher thermal inputs, the morphology of these second phases is more equiaxed in acicular ferrite (Figures 6(b) and 7(b)). In addition, it is important to note that the morphology of these interlath particles depends not only on the welding energy but also on the silicon content of the steel. For instance, Figure 7 shows that these secondary constituents display an unbroken appearance consistent with their whole austenitic nature in the most Si-alloyed steel (Steel D) simulated at low heat inputs. On the contrary, at high welding energies, the secondary constituents tend to exhibit a divorced morphology due to the partial decomposition of austenite in pearlite. With the reduction of the silicon level of the steels, the latter transformation is amplified and takes place at lower heat input (Figure 7). The monophased parts of these second phases were identified as austenite by thin foil TEM (as shown in the γ micrograph in Figure 7(b)), X-ray diffractometry, and MS (Figure 8) investigations. For instance, Figure 8 displays typical Mössbauer spectra obtained with the highest and lowest Si-alloyed materials simulated at high heat input (Δt = 120 s). Over the ±9-mm/s velocity

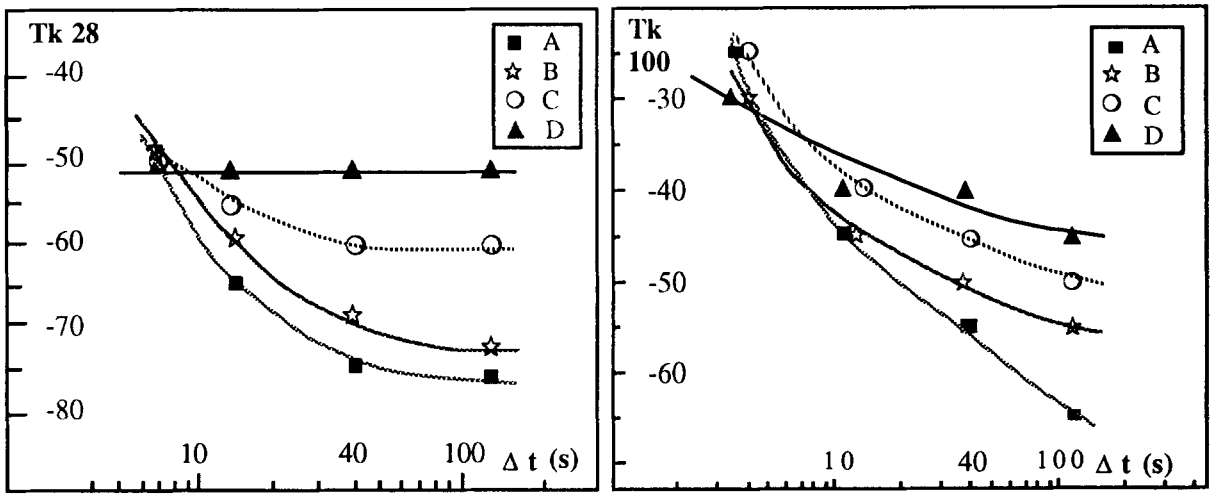

(*a*) (*b*)

Fig. 4—Effect of welding energy, or Δt (Table III), on the Charpy V transition temperature at a fracture energy of (*a*) 28 J (Tk28) and (*b*) 100 J (Tk100).

range, the spectra exhibit the three central peaks of austenite plus six twinned peaks of ferrite. The peaks of ferrite correspond to the 0^{α} and I^{α} iron atoms' surroundings. The I^{α} and 0^{α} sites are defined respectively by the presence or absence of one substitutional atom, other than iron, on the sphere of the nearest substitutional localizations from an atom of iron. In the present work, these atoms are either Si or Mn, because with regard to the steel chemical composition, they are the only elements that exert a significant effect on the iron internal field.[15,16] In a similar way, the peaks of austenite arise from the 0^{γ} and I^{γ} iron atoms surroundings. The 0^{γ} and I^{γ} sites indicate, respectively, the missing and the presence of one carbon atom on the sphere of the nearest interstitial localizations from an atom of iron.

In general, the existence of austenitic second phases in a ferritic matrix may arise from two origins. First, in the case of an M_f value lower than room temperature, the austenite results from incomplete transformation (residual austenite). Second, the austenite can be retained as a result of chemical and/or mechanical stabilization. The retained origin of austenite is self-evident from the nearly 400 °C M_s temperature of close-compositioned steels.[4,9,17] As suggested by Figure 7, the stability of retained austenite is closely connected to the silicon content of the steels. At high heat inputs, retained austenite is essentially completely decomposed in pearlite in low-Si steel A (Figure 7(a)), whereas this pearlitic transformation is only partial in high-Si-alloyed steel D (Figure 7(b)). In accordance with these observations, Figure 9 shows that the effect of welding energy on the retained austenite volume fraction depends on the level of silicon in the alloys. The lowest Si-alloyed steels (A and B) exhibit a continual decrease of the retained austenite volume fraction with Δt, contrary to high-Si steels C and D, which display maxima in the volume fraction of retained austenite over the Δt range. In addition, it is relevant that the cooling time corresponding to these maxima decreases with the silicon content of the material. Furthermore, Figure 10 demonstrates the evolution of the average carbon content of retained austenite with Δt. Both the high carbon concentration in retained austenite and the close similarity between the responses of γr pct and of $(C\ pct)_{\gamma}$ to Δt (Figures 9 and 10) must be emphasized. The present estimates of the carbon content of retained austenite were obtained from area measurements of the 0^{γ} and I^{γ} peaks of the Mössbauer spectra.[12] Figure 10 displays that the level of carbon in retained austenite is far higher than that of the base plates. For instance, the carbon enrichment of retained austenite is so pronounced that the 5 pct volume fraction of retained austenite present in steel D at a Δt of 40 seconds contains as much as 33 pct of the total carbon content of the alloy. In addition to its ability to estimate $(C\ pct)_{\gamma}$, MS is also a very potent tool for investigation of the partitioning silicon between austenite and ferrite. In this work, the area of the I^{α} peak increases proportionally to the concentration of silicon in the alloy.[6] Moreover, Figure 11 shows that, for all heat inputs, the relative areas [$A\alpha$ pct] of 0^{α} and I^{α} remain constant in a given alloy. These latter data prove that the welding operation exerts no effect on the substitutional content of ferrite. It generalizes our previous EDX analyses[6,9,18] and the ion probe or scanning transmission electron microscopy (STEM) and EDX investigations of other authors[19,20] of higher alloyed steels, according to which the Mn and Si contents of austenite and ferrite remain constant during high temperature quenching.

Furthermore, it is worth noting that the propensity toward intragranular precipitation of cementite is retarded by increasing the Si content of the alloy. This feature is illustrated by the transmission electron micrograph of Figure 12 that exhibits a noticeable volume fraction of intragranular particles of Fe_3C, with the conventional Bagaryatsky orientation relationships with the ferritic matrix in the least-Si-alloyed steel (A) at the lowest heat input. On the contrary, there is no intragranular precipitation of cementite in the highly Si-alloyed steel (D), and this even after the longest cooling times. In addition to the possibility of intragranular

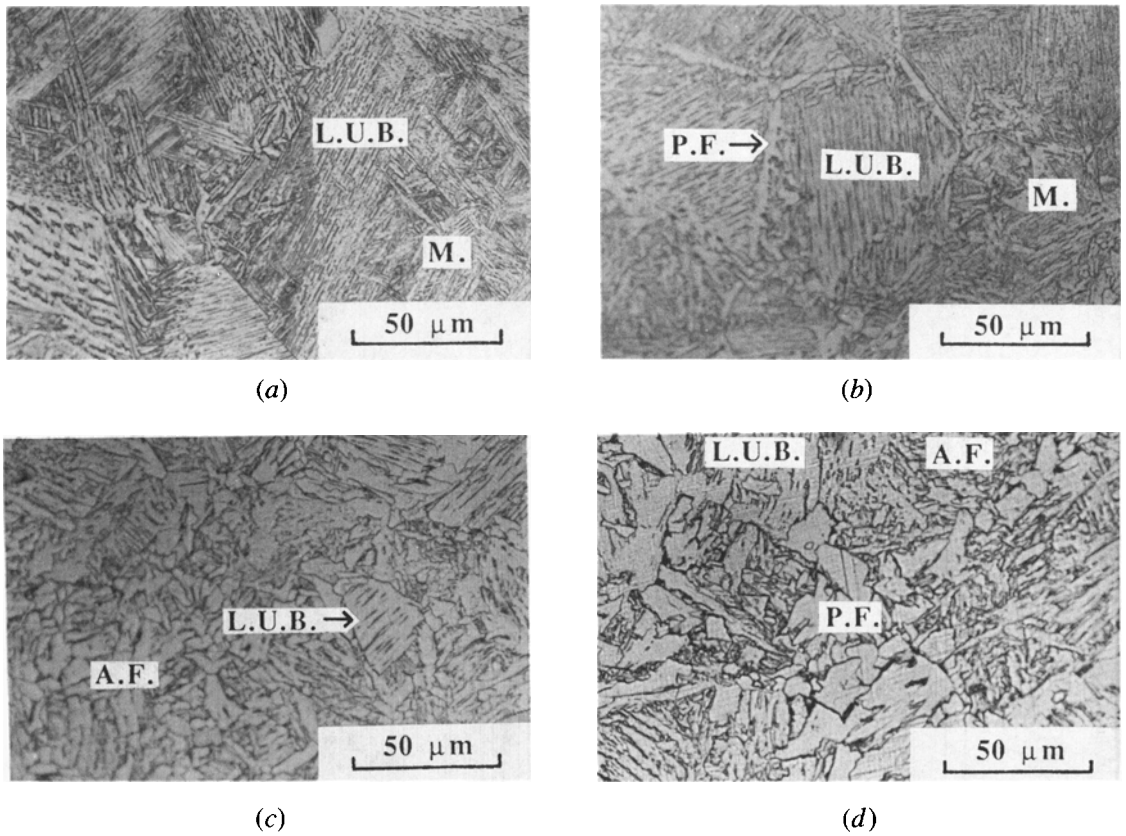

Fig. 5—Light micrographs showing the evolution of the microstructure of steel B with Δt: (*a*) Δt = 4 s, (*b*) Δt = 12 s, (*c*) Δt = 40 s, and (*d*) Δt = 120 s.

Table IV. CGHAZ Microstructure (Area Fractions, Percent)

	A				B				C				D			
Δt	4	12	40	120	4	12	40	120	4	12	40	120	4	12	40	120
M	45	15	—	—	50	20	—	—	55	35	—	—	55	35	—	—
LUB	50	70	20	10	45	70	25	15	40	60	40	20	45	60	35	20
AF	—	5	60	70	—	—	55	65	—	—	45	60	—	—	50	60
PF	5	10	20	20	5	10	20	20	5	5	15	20	—	5	15	20

M: martensite, LUB: lath upper bainite, AF: acicular ferrite, PF: proeutectoid ferrite.

carbides and at any welding energy, the steels contain a homogeneous distribution of cuboidal particles with a 60-nm mean edge length. These precipitates possess a face centred cubic (fcc) crystallography with a 0.42-nm lattice parameter. According to this crystallography[10] and the steel's chemical composition, these precipitates are very likely of the TiN type. The marked resistance of these TiN particles to dissolution during a weld thermal cycle[10] appears to explain the constancy of the prior austenite grain size by their pinning action on the grain boundaries.[21]

IV. DISCUSSION

This section discusses the effect of silicon upon the mechanical behavior of the CGHAZ for laboratory alloys A through D. The significance of silicon for the microstructure and the microstructural dependence of the mechanical properties are successively discussed, with the outcome of the definition of an optimum silicon content.

A. *Effect of Silicon on the CGHAZ Microstructure*

Table IV and Figure 3 exhibit a slight improvement in hardenability with increasing silicon content. This well-known feature[22] is usually explained by the retardation of the diffusional decomposition of austenite by silicon.[23]

Furthermore, the results of TEM (Figure 7), X-ray diffractometry (Figure 9) and MS indicate an increase in the stability of retained austenite with the silicon content of the steels. As suggested by Figure 10, this phenomenon arises, at least in part,* from the increases in the

*Aside from its carbon enrichment, the compressive strains due to the $\gamma \rightarrow \alpha$ phase transformation of the surrounding areas may additionally contribute to the stabilization of austenite.

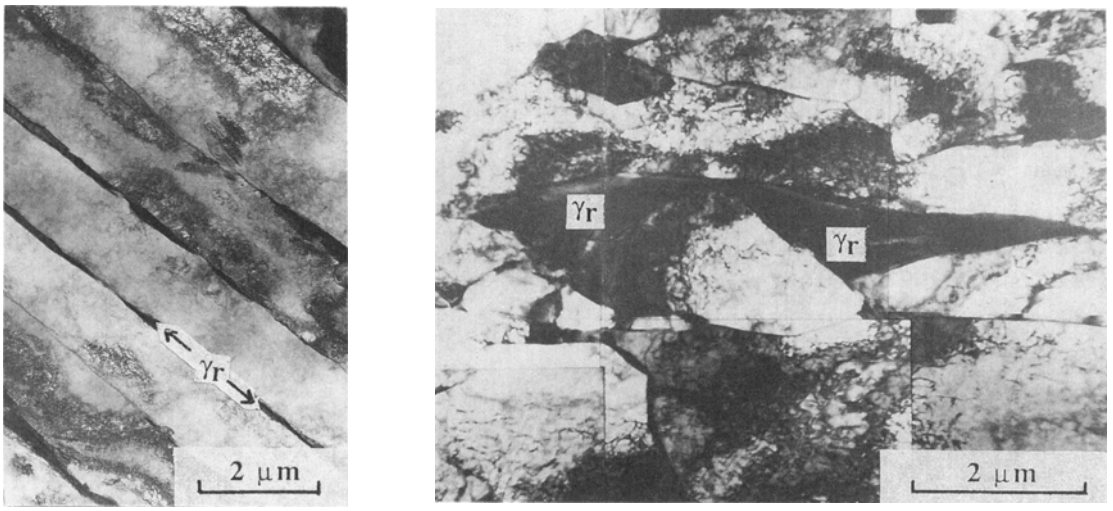

(*a*) (*b*)

Fig. 6—Typical thin-foil electron micrographs displaying the predominant microstructural constituent in steel D: (*a*) lath upper bainite (Δt = 12 s) and (*b*) acicular ferrite (Δt = 120 s).

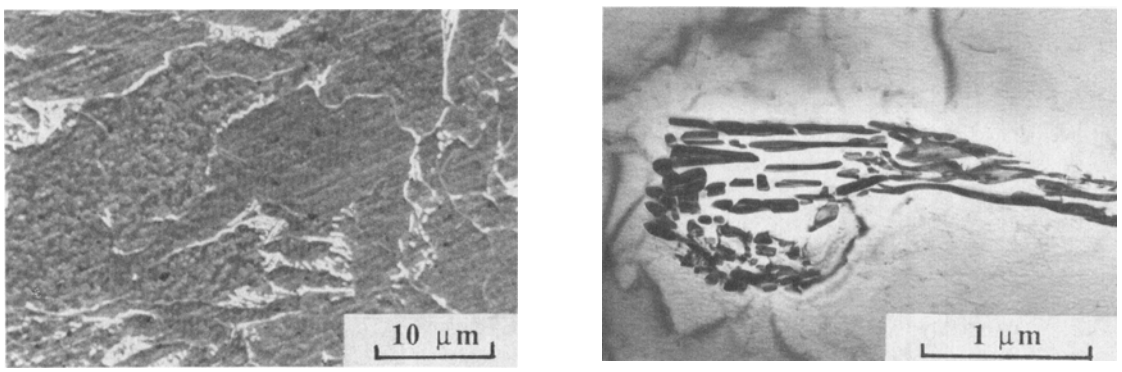

α – Δt = 40s β – Δt = 120s

(*a*) Si = 0.050 wt %.

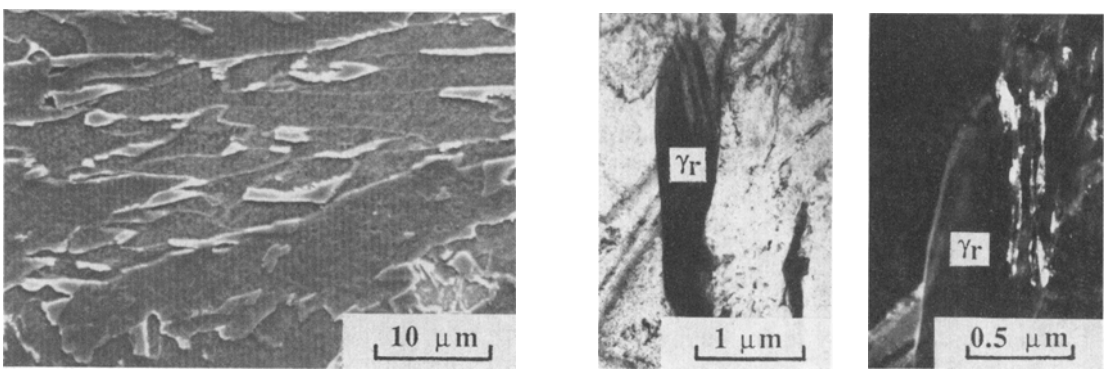

α – Δt = 40s β Δt = 120s γ Δt = 120s

(*b*) Si = 0.500 wt%.

Fig. 7—Degree of decomposition of retained austenite in pearlite in (*a*) less Si-alloyed steel A and (*b*) most Si-alloyed steel D: (*α*) SEM, (*β*) bright-field TEM, (*γ*) dark-field TEM.

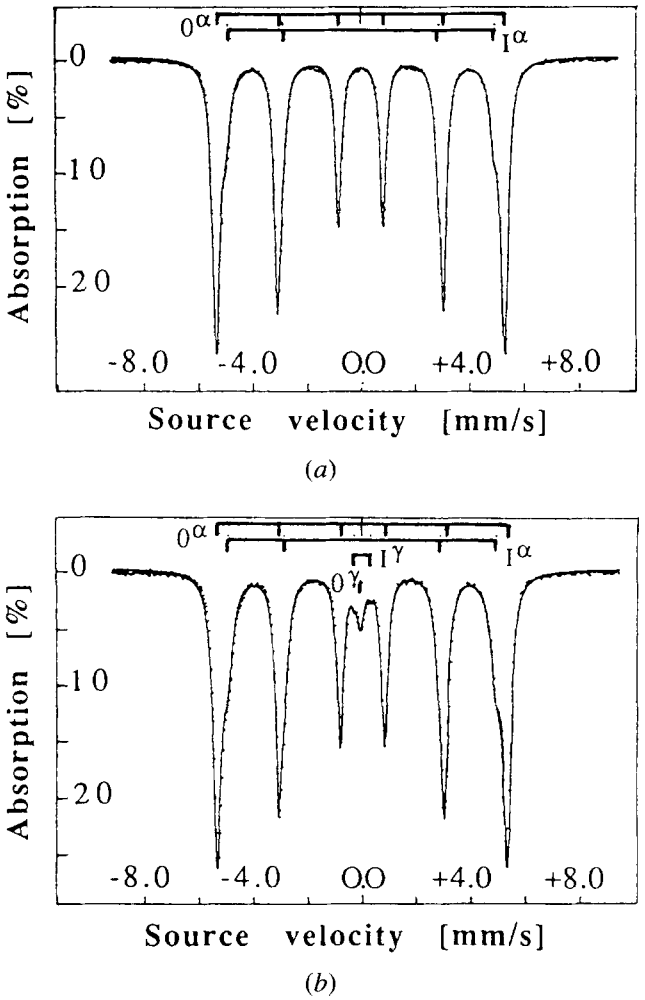

Fig. 8—Typical spectra of nuclear gamma resonance at the ±9 mm/s velocity range for (*a*) steel D (Δt = 120 s) and (*b*) steel A (Δt = 120 s).

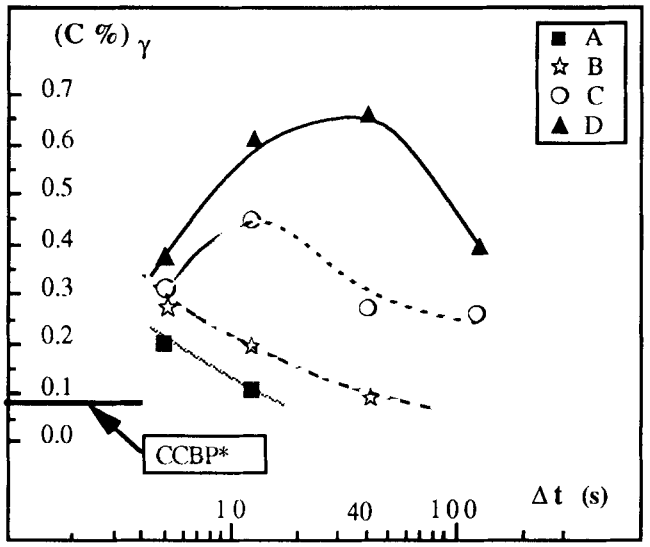

Fig. 10—Effect of welding energy and of the silicon content of the alloy on the weight percentage of carbon in retained austenite. *CCBP: carbon content of the base plates.

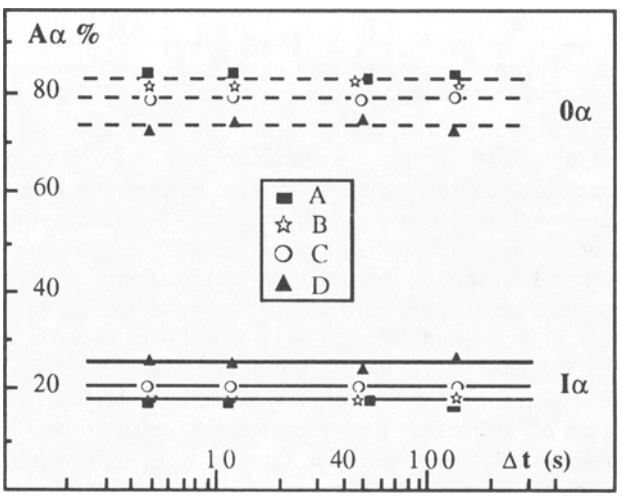

Fig. 11—Effect of welding energy on the areas of the 0^α and I^α peaks.

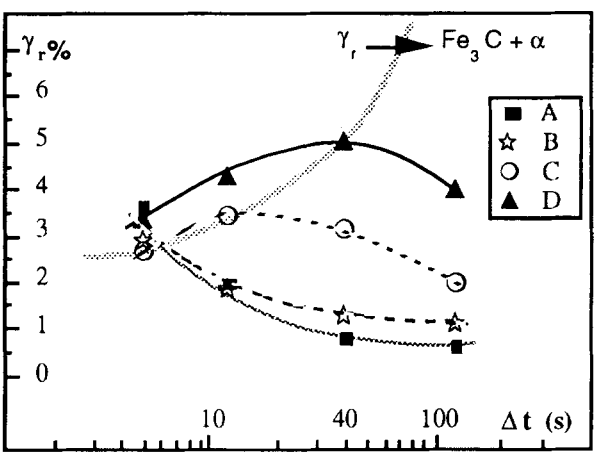

Fig. 9—Effect of cooling time and of silicon content on the X-ray estimates of the retained austenite volume fraction (γr pct).

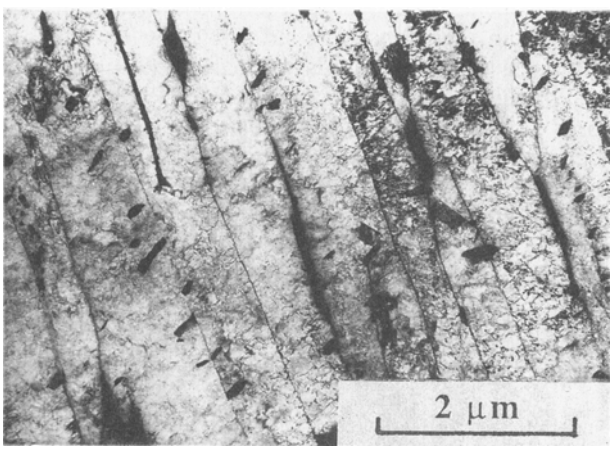

Fig. 12—Typical aspect of the Fe_3C intralath precipitation in steel A simulated at Δt = 4 s.

carbon content of retained austenite with increasing silicon content. Moreover, it is important to consider the results of the EDX and MS analyses, according to which the chemical composition of retained austenite differs only from that of ferrite by its carbon enrichment. The effect of silicon on the carbon content of retained austenite will now be discussed with reference first to the $\gamma \rightarrow \alpha$ phase transformation and then to the hindrance of the pearlitic decomposition of austenite.

The increase of the carbon concentration in retained austenite due to the $\gamma \rightarrow \alpha$ allotropic reaction is amplified by the action of the silicon atoms in substitutional solid solution in ferrite. The Si atoms prevent the precipitation of cementite[24] with the logical consequence of the carbon enrichment of undersaturated austenite. It should be noted that this effect of silicon can be anticipated from Hultgren's extrapolations to low temperature of the Fe-C-Si equilibrium phase diagrams.[25,26]

As a consequence of the Si in solid solution in ferrite, the highest Si-alloyed steels (C and D) exhibit an increase in the carbon content of the retained austenite with cooling time (Figure 10). The phenomenon is effective at cooling times up to 12 and 40 seconds in alloys C and D, respectively. In these latter conditions, the increase of welding energy promotes the diffusion of carbon from ferritic to austenitic areas, with the consequence of the stabilization of austenite (Figure 9). Furthermore, it is important to note the shift of the maxima of $(C\ pct)_\gamma$ toward high cooling times with increasing silicon content (Figure 10). In close correspondence with this feature, Figures 7 and 9 indicate that the pearlitic decomposition of γr is more or less complete at high heat inputs. Retained austenite is therefore more prone to transform by diffusional mechanisms, the lower the silicon content of the alloy. For instance, and for the extreme case of the lowest Si-alloyed steels (A and B), the volume fraction of retained austenite decreases because of its partial decomposition in pearlite from the lowest thermal inputs. In the same way, at high welding energies, the retained austenite volume fraction increases with the concentration of silicon in the material. Moreover, it is worthwhile to note by comparing Figure 9 with Figure 10 the concomitant decreases of the volume fraction and carbon content of retained austenite due to its pearlitic decomposition. To conclude, it is apparent from these observations that the silicon in solid solution in austenite retards its pearlitic decomposition. This effect of silicon has been noted by several authors[27,28] for steels with similar compositions. Two mechanisms are proposed for this retardation. First, the silicon in austenite impedes the diffusion of carbon[24] and, therefore, slows down the formation of the carbides. On the other hand, the diffusion-controlled growth of carbides is counteracted by the presence of an Si-enriched layer around the precipitate nuclei.[29,30,31]

B. *Effect of Microstructure on Mechanical Behavior*

1. *Hardness*

As exhibited by Figure 3, the CGHAZ softens with an increase of the welding energy at constant silicon content. This relationship results from the evolution of the microstructure displayed in Table IV. The highest hardness, achieved at $\Delta t = 4$ s, corresponds to a duplex microstructure comprised of martensite and lath upper bainite. The increase in welding energy leads to a decrease in hardness because of the transformation of the microstructure from a mixture of martensite and bainite into the softer acicular and proeutectoid ferrite. It should be noted that similar correlations already have been established for similar steels by a number of authors.[2,4–6,32,33]

At constant cooling time, the hardness increases in progression from steel A to steel D. As shown by Table IV, this feature is the result of the hardenability potential of silicon.[23]

In addition, with reference to the 325 to 400 Hv5 level observed at the lowest cooling times for the 0.1 pct C niobium microalloyed steels,[4,5,6] it is important to notice the low hardenability of steels A through D (Figure 3). This lack of hardenability arises from the reductions of carbon and silicon concentrations that bring about a decrease of the martensite volume fraction.[22]

2. *Toughness*

As previously reported by the authors,[4–7] the CGHAZ toughness of microalloyed steels is predominantly impaired by the retained austenite volume fraction. For instance, Figure 13 shows that this effect corresponds to an increase of Tk28 equal to +14 and +8 K per volume percent of retained austenite in a ferrite side plates structure and in acicular ferrite, respectively. Conversely, acicular ferrite exerts a beneficial effect on the CGHAZ toughness through the decrease of the ferritic grain size and through the reduction of the stress-raising effect resulting from the decrease of sharpness of retained austenite particles. The present discussion of the effect of microstructure on the CGHAZ toughness of synthetic alloys A through D is based on these two observations.

At the shortest cooling time of 4 s (lowest welding energy) and at any silicon content, Tk28 is close to −50 °C (Figure 14). This steady behavior is in good agreement with the constant volume fraction of retained austenite shown in Figure 15. Moreover, Figure 14 shows that the toughness of the lowest Si steels (A and B) is improved by an increase of heat input. According to Figures 7 and 15, this improvement results from the pearlitic decomposition of retained austenite. In particular, the more complete the austenite decomposition is, the more improved is the toughness (compare Figures 14 and 15). This observation demonstrates that pearlite is less detrimental than retained austenite on the toughness of microalloyed steels.

Alternatively, for high-silicon steel D, the degradation of toughness with welding energy is lower than would be expected from increases in volume fraction of retained austenite alone. In this case, the deleterious influence of retained austenite is offset by the increase of the volume fraction of acicular ferrite (Table IV).

To conclude, it is important to note that the present results fit the linear regressions between Tk28 and the retained austenite volume fraction (Figure 13). This agreement confirms the predominant and harmful effect of retained austenite on the CGHAZ toughness of these microalloyed steels. In particular, pearlite is less harmful

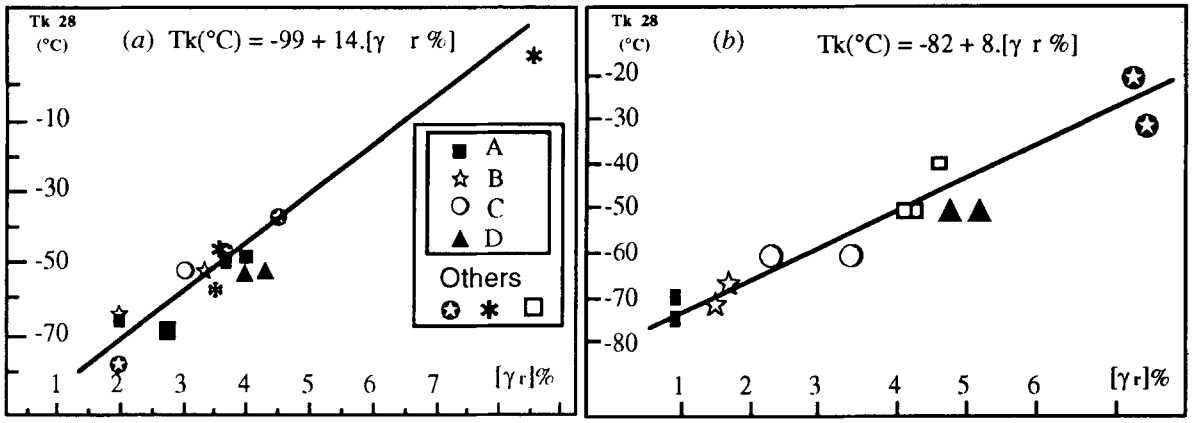

Fig. 13—Effect of the volume fraction of retained austenite on the Tk28: (*a*) ferritic side plates structure and (*b*) acicular ferrite.

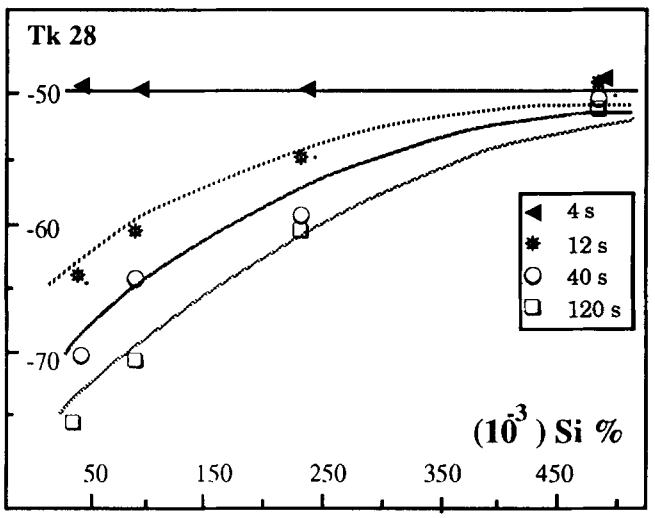

Fig. 14—Correlation between the silicon content and the Charpy V transition temperature of the CGHAZ.

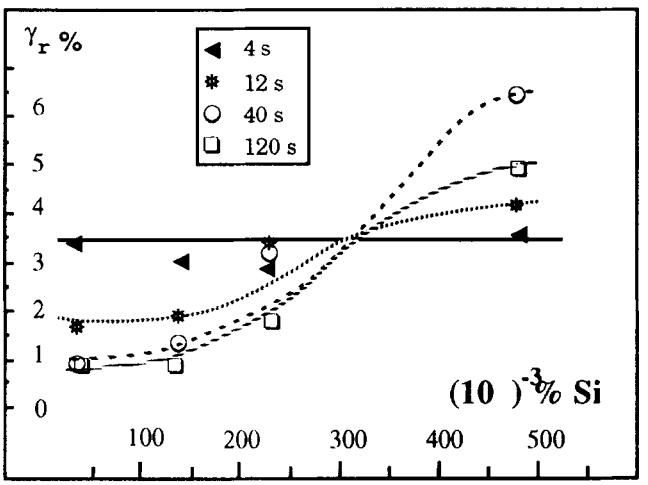

Fig. 15—Effect of the silicon content on the volume fraction of γr.

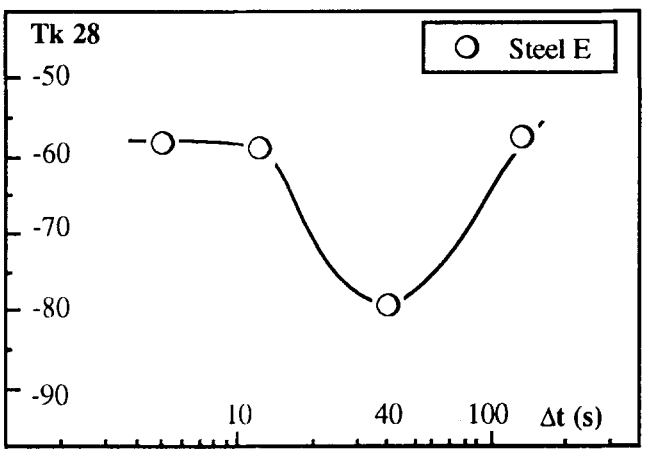

Fig. 16—Relationship between Tk28 and Δt.

than retained austenite, and, as suggested by the behavior of alloy A and ascertained by the literature data,[34] thin intergranular carbides (<0.1 μm) exert only a weak influence on the toughness of a ferritic material with a grain size finer than 80 μm.

C. *Optimum Silicon Content*

In accordance with the predominant effect of retained austenite on toughness, Figure 15 shows that the silicon concentration must be lower than 0.100 to 0.150 wt pct. However, this silicon content must not be too low in order to maintain the tensile properties of the base metal (Table II). Both conditions lead to the choice of a 0.100 wt pct Si content in steel E. The study of this industrial heat has the advantage of verifying the previous results obtained with laboratory alloys.

Figure 16 shows that steel E displays very good toughness following the CGHAZ simulations. At any welding energy, the Tk(28) transition temperature is never higher than −60 °C. The best result is achieved for Δt = 40 s, for which Tk28 is close to −80 °C. This high level of toughness of the CGHAZ is in agreement with its low volume fraction of retained austenite that never exceeds $2.5 \cdot 10^{-2}$ (Figure 17).

The decrease of Tk with Δt over the [4 s, 40 s] range is closely correlated to the reduction of the retained austenite volume fraction (Figure 17) and to the formation of acicular ferrite[2,4,6,8] (Table V). In contrast, for Δt =

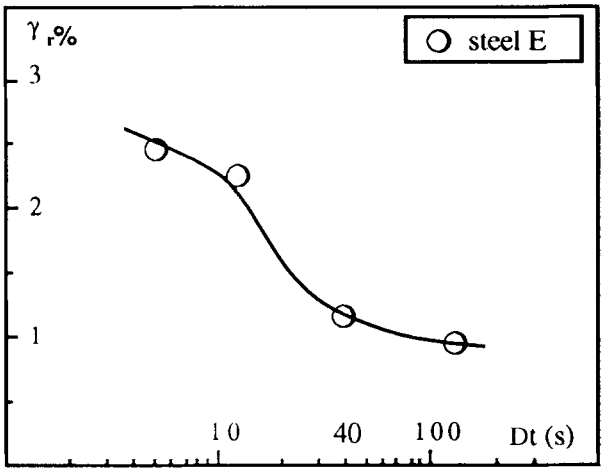

Fig. 17—Effect of Δt on the γr volume fraction in the CGHAZ of steel E.

Table V. Evolution of the CGHAZ Microstructure (Area Fractions Percent) of Steel E, with Δt

Δt (s)	4	12	40	120
LUB	95	70	5	—
AF	—	20	80	80
PF	5	10	15	20
$d\alpha$ (μm)	—	—	10	16

LUB: lath upper bainite, AF: acicular ferrite, PF: protectoid ferrite, $d\alpha$: ferritic grain size

120 s, the expected toughness improvement that might result from the decrease of the retained austenite volume fraction is not observed. This effective lowering of toughness can be explained by the increases of both the ferritic grain size[6,35] and volume fraction of proeutectoid ferrite (Table V), and by the presence of intergranular carbides with a close to 0.3 μm thickness in the samples cooled for 120 s.[6,34,35]

To conclude, the results show the advantage of a fine acicular ferritic structure with a low volume fraction of retained austenite for the CGHAZ toughness of 0.1 wt pct C microalloyed steels. This optimum microstructure may arise from a reduction of the silicon concentration to about 0.1 to 0.15 wt pct in Ti-optimized alloys. In addition, it is important to note that this beneficial effect of a low silicon content on toughness was further verified in both the intercritical and the coarse-grained heat-affected parts of real weld joints.[6] Moreover, a reduction of the silicon content leads also to an improvement of the cold-cracking resistance of the CGHAZ because of the lowering of its hardenability.[6]

V. CONCLUSIONS

This investigation of Ti-microalloyed steels of the E 355 grade has demonstrated the need to consider the microstructure in order to understand the effects of welding energy and/or chemical composition on the mechanical behavior of weldments.

The study of the simulated CGHAZ of laboratory heats shows that an increase of the silicon content brings about:

1. a slight enhancement of the hardenability of the steels because of the retardation of carbon diffusion.
2. an overall increase in retained austenite volume fraction that is more pronounced at high welding energy. This stabilization of austenite arises from its high carbon content due to the hindrance of the formation of Fe_3C precipitates in ferrite as well as in austenite.

The mechanical properties of the CGHAZ are directly related to these modifications of the microstructure. The hardness depends on the kind and volume fraction of the various microstructural constituents. The variations of toughness arise primarily from the deleterious influence of the retained austenite volume fraction. This effect on the transition temperature amounts to +14 and +8 K per volume percent of retained austenite in ferritic side plates and acicular ferrite structures, respectively. These correlations explain the present and unusual increase of toughness with an increase of welding energy because of the decomposition of austenite in pearlite in the less Si-alloyed materials. All these results show the advantage of a fine acicular ferritic microstructure with a low volume fraction of retained austenite.

NOTATION

AF	acicular ferrite
CGHAZ	coarse-grained heat-affected zone
$(C\ pct)_\gamma$	weight percentage of carbon in retained austenite
Δt	cooling time between 1073K (800 °C) and 773K (500 °C)
EDX	energy dispersive X-ray analysis
γr pct	retained austenite volume fraction
HAZ	heat-affected zone
Hv	Vickers' hardness number
LUB	lath upper bainite
M	martensite
MS	Mössbauer spectrometry
PF	proeutectoid ferrite
SEM	scanning electron microscopy
STEM	scanning transmission electron microscopy
TEM	transmission electron microscopy
Tk(X)	Charpy V transition temperature at a fracture energy of X joules
Tp	welding peak temperature

REFERENCES

1. K.E. Easterling: *Introduction to the Physical Metallurgy of Welding*, Butterworth and Co., London, 1983, pp. 104-218.
2. M. Toyoda: Osaka University Report, Part I and II, Osaka, Japan 1988.
3. D. Rosenthal: *Trans. ASME*, 1946, vol. 68, pp. 849-62.
4. P. Verrier, T. Maurickx, R. Taillard, and G. Guarrigues: *8th Int. Conf. on Offshore Mechanics and Arctic Engineering*, ASME, New York, NY, 1989, pp. 641-47.
5. R. Taillard, J. Foct, P. Verrier, and T. Maurickx: *The Martensitic Transformation in Science and Technology*, E. Hornbogen and N. Jost, eds., Bochum, Germany, 1989, pp. 495-502.
6. P. Verrier: Doctoral Thesis, University of Lille I, France, 1990.

7. R. Taillard, P. Verrier, T. Maurickx, and J. Foct: *Welding '90*, M. Koçak ed., I.I.T.T., Paris, 1990, pp. 229-36.
8. J.H. Chen, Y. Kikata, T. Araki, M. Yoneta, and Y. Matsuda: *Acta Metall.*, 1984, vol. 32, pp. 1779-88.
9. T. Maurickx: Doctor Eng. Thesis, University of Lille I, France, 1987.
10. T. Maurickx and R. Taillard: *High Nitrogen Steels '88*, J. Foct and A. Hendry, eds., The Institute of Metals, London, 1988, pp. 327-32.
11. N.E. Hannerz: Report No. 70-728/U 615, Swedish Board of Technical Development, Stockolm, 1972.
12. T. Maurickx, R. Taillard, and J. Foct: *C.R. Acad. Sci.*, 1986, vol. 303, series II, pp. 41-46.
13. O.M. Akselsen, O. Grøng, and J.K. Solberg: *Mater. Sci. Technol.*, 1987, vol. 8, pp. 649-55.
14. Y. Kasamatsu, S. Takashima, and T. Hosoya: *J. Iron Steel Inst. Jpn.*, 1979, vol. 25, pp. 92-101.
15. J.H. Ladriere and X.J. He: *Mater. Sci. Eng.*, 1986, vol. 77, pp. 133-38.
16. T.E. Cranshaw, B.W. Dale, G.O. Longworth, and C.E. Johnson: *Mössbauer Spectrometry and its Applications*, Cambridge University Press, Cambridge, U.K., 1985, pp. 69-76.
17. K.W. Andrews: *J. Iron Steel Inst. London*, 1965, vol. 203, pp. 721-27.
18. R. Taillard, T. Maurickx, and J. Foct: *Electron Microscopy and Analysis*, Institute Physics Conference Series, Adam Hilger Ltd., London, 1985, pp. 391-94.
19. M. Sarikaya, G. Thomas, and J.W. Steeds: *Solid-solid Phase Transformations*, H.I. Aaronson, D.E. Laughlin, R.F. Sekerka, and C.M. Wayman, eds., TMS-AIME, Warrendale, PA, 1981, pp. 1421-25.
20. A.D. Romig and R. Salzbrenner: *Solid-solid Phase Transformations*, H.I. Aaronson, D.E. Laughlin, R.F. Sekerka, and C.M. Wayman, eds., TMS-AIME, Warrendale, P.A., 1981, pp. 849-53.
21. L.J. Cuddy and J.C. Raley: *Metall. Trans. A*, 1983, vol. 14A, pp. 1989-95.
22. A. De Sy and J. Vidts: *Métallurgie Structurale*, Dunod, Paris, 1968, 2nd ed., pp. 352-353.
23. I. Tamura, C. Ouchi, T. Tanaka, and H. Sekine: *Thermomechanical Processing of High Strength Low Alloy Steels*, Butterworth and Co., London, 1988, pp. 17-18.
24. J. Pomey: *Rev. Métall., M.T.*, 1966, vol. LXIII, pp. 509-532.
25. A. De Sy and J. Vidts: *Métallurgie Structurale*, Dunod, Paris, 1968, 2nd ed., pp. 297-303.
26. J.S. Kirkaldy, B.A. Thomson, and E.A. Baganis: *Hardenability Concepts with Applications to Steel*, D.V. Doane and J.S. Kirkaldy, eds., TMS-AIME, Warrendale, PA, 1978, pp. 82-125.
27. H.C. Chen, H. Era, and M. Shimizu: *Metall. Trans. A*, 1989, vol. 20A, pp. 437-55.
28. S.K. Liu, W.T. Reynolds, H. Hu, G.J. Shiflet, and H.I. Aaronson: *Metall. Trans. A*, 1985, vol. 16A, pp. 457-67.
29. S.J. Barnard, G.D.W. Smith, A.J. Garratt-Reed, and J. Vander Sande: *Solid-solid Phase Transformations*, H.I. Aaronson, D.E. Laughlin, R.F. Sekerka, and C.M. Wayman, eds., TMS-AIME, Warrendale, P.A., 1981, pp. 881-85.
30. H.K.D.H. Badeshia and D.V. Edmonds: *Metall. Trans. A*, 1979, vol. 10A, pp. 895-907.
31. P.R. Williams, M.K. Miller, and G.D.W. Smith: *Solid-solid Phase Transformations*, H.I. Aaronson, D.E. Laughlin, R.F. Sekerka, and C.M. Wayman, eds., TMS-AIME, Warrendale, P.A., 1981, pp. 813-17.
32. G. Bernard: *Cahiers d'Informations Techniques*, Institut de Recherches de la Sidérurgie Française, Saint Germain en Laye, France, 1979, vol. 2, pp. 249-65.
33. O.M. Akselsen, Ø. Grong, and P.E. Kvaale: *Metall. Trans. A*, 1986, vol. 17A, pp. 1529-36.
34. N.J. Petch: *Acta Metall.*, 1986, vol. 34, pp. 1387-93.
35. Y. Tomita and O. Okabayashi: *Metall. Trans. A*, 1986, vol. 17A, pp. 1203-09.